Joule

CellPress

Report

Efficient Direct Recycling of Lithium-Ion Battery Cathodes by Targeted Healing

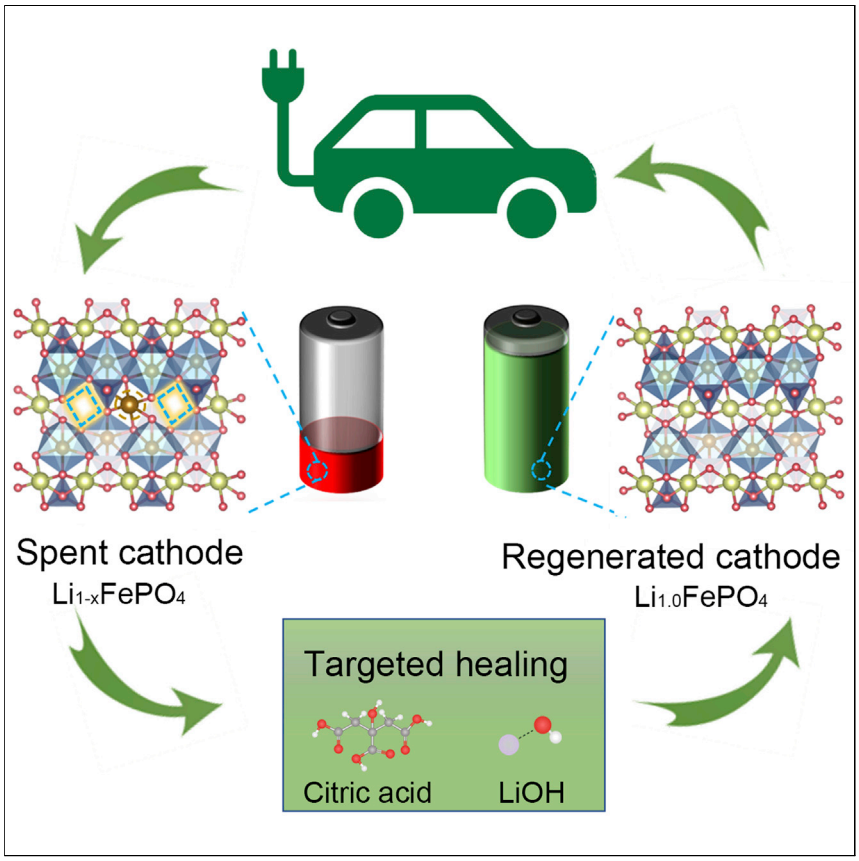

A paradigm-shift lithium-ion battery recycling method based on defect-targeted healing can fully recover the composition, structure, and electrochemical performance of spent $LiFePO_4$ cathodes with various degradation conditions to the same levels as that of the pristine materials. Such a direct recycling approach can significantly reduce energy usage and greenhouse gas emissions, leading to significant economic and environmental benefits compared with today's hydrometallurgical and pyrometallurgic methods. This work may pave the way for industrial adoption of directly recycled lithium-ion battery materials.

Panpan Xu, Qiang Dai, Hongpeng Gao, ..., Linda Gaines, Jun Lu, Zheng Chen

zhengchen@eng.ucsd.edu

HIGHLIGHTS

A safe and low-cost method was developed to directly recycle $LiFePO_4$ cathodes

A targeted healing strategy can fully resolve composition and structure defects

The regenerated cathode reached the same performance of pristine $LiFePO_4$ materials

Direct recycling shows dramatically improved economic and environmental benefits

Xu et al., Joule 4, 1–18
December 16, 2020
https://doi.org/10.1016/j.joule.2020.10.008

Please cite this article in press as: Xu et al., Efficient Direct Recycling of Lithium-Ion Battery Cathodes by Targeted Healing, Joule (2020), https://doi.org/10.1016/j.joule.2020.10.008

Joule

CellPress

Report

Efficient Direct Recycling of Lithium-Ion Battery Cathodes by Targeted Healing

Panpan Xu,[1] Qiang Dai,[2] Hongpeng Gao,[3] Haodong Liu,[1] Minghao Zhang,[1] Mingqian Li,[1,6] Yan Chen,[4] Ke An,[4] Ying Shirley Meng,[1,3,5] Ping Liu,[1,3,5,6] Yanran Li,[7] Jeffrey S. Spangenberger,[8] Linda Gaines,[2] Jun Lu,[9] and Zheng Chen[1,3,5,6,10,*]

SUMMARY

Recycling of spent lithium-ion batteries (LIBs) is an urgent need to address their environmental and global sustainability issues. Here, we report an efficient and environmentally benign LIB regeneration method based on defect-targeted healing, which represents a paradigm-shift LIB recycling strategy. Specifically, by combining low-temperature aqueous solution relithiation and rapid post-annealing, we demonstrate successful direct regeneration of spent $LiFePO_4$ (LFP) cathodes, one of the most important materials for EVs and grid storage applications. We show revitalization of composition, structure, and electrochemical performance of LFP with various degradation conditions to the same levels as the pristine LFP. Life-cycle analysis of different LIB recycling processes shows that this defect-targeted direct reycling approach can significantly reduce energy usage and greenhouse gas (GHG) emissions, leading to more economic and environmental benefits compared with today's hydrometallurgical and pyrometallurgical methods.

INTRODUCTION

Olivine lithium iron phosphate ($LiFePO_4$ or LFP) is one of the most widely used cathode materials for lithium-ion batteries (LIBs), owing to its high thermal stability, long cycle life, and low-cost. These features make the LFP battery share more than one third of the entire LIB market, currently dominating applications in power tools, electric bus, and grid energy storage.[1] The global demand of LIBs is projected to reach 440 GWh in 5 years.[2] As a result, millions of tons of spent LIBs will soon be generated after their service lives (3 to 10 years). Effective recycling and remanufacturing of spent LIBs can help to reclaim valuable materials, reduce energy use for mining of natural resources, and mitigate environmental pollution from the end-of-life management of waste batteries, making LIBs more affordable and sustainable.

Current efforts on LIB recycling have focused mainly on the recovery of valuable metals. For example, pyrometallurgical and hydrometallurgical processes have been commercially used to recycle LIBs containing cobalt (Co) and nickel (Ni). These processes generally involve battery dismantling, smelting, and/or acid leaching followed by multi-step chemical precipitation and separation, finally breaking LIB cells down into simple compounds (e.g., $CoSO_4$, $NiSO_4$, Li_2CO_3) that can be used to resynthesize new cathode materials.[3] Due to the high value of transition metals (e.g., ~$30/kg for Co),[4] a reasonable economic return can be achieved from such recycling processes, despite their high operating costs. However, their intensive usage of

Context & Scale

The consumption of lithium-ion batteries is experiencing booming growth in the modern industry due to their widespread applications. With billions of batteries reaching their lifetime soon, significant concerns on the economic and environmental issues have been raised about how to treat these spent batteries so that our society will not face similar crisis incurred in the case of plastic wastes. However, traditional technologies used in today's recycling industry are limited to recovering expensive metals through energy-intensive processes, which cause significant greenhouse gas emissions and secondary wastes, posing additional environmental concerns. To tackle this challenge, we developed a safe, low-cost, and efficient direct recycling approach that is based on targeted healing. This paradigm-shift method leverages our understanding on phase and structure evaluations of the LIB cathode and produces ready-to-use recycled cathode materials that match the electrochemical performance of pristine materials.

energy and chemicals (acids, oxidation reagents) causes significant greenhouse gas (GHG) emissions and secondary wastes, posing additional environmental concerns. Moreover, a large portion of the cathode's value, represented by their tailored composition and structure, is completely lost from these destructive recycling processes. Therefore, more efficient approaches with significantly reduced energy cost and waste generation are needed, especially for LIBs made without expensive metals, such as LFP, as the economic value of their recycled elemental products is insufficient to compensate for the high cost of pyrometallurgical and hydrometallurgical processes.[4] This is particularly true when considering the fact that the world battery makers have been producing about 100,000 tons year^{-1} of LFP cathodes in total, since 2015.[5] The large quantity of these batteries that will soon be retired urgently calls for better recycling solutions.

Decades of studies have uncovered that the performance degradation of LFP cathode is mainly attributed to Li vacancy defects (Li_v) and Fe occupation of Li site (Fe_{Li}).[6,7] The Li_v defects not only result in the oxidation of Fe^{2+} to Fe^{3+} but also induce partial migration of Fe^{2+} to lithium site, forming the so-called "anti-site" defects, which block the Li^+ diffusion pathway (Figure 1A). While there may be a significant loss in the charge storage capacity, the morphology and bulk crystal structure of spent LFP particles often remain unchanged. This failure mechanism provides a potential opportunity to directly revitalize degraded LFP to form new LFP particles that can be readily used in making new battery cells. It can be expected that such a simple process requires much less energy and chemical input to recycle spent cells. In addition, the value of embodied energy in the electrode active materials will be retained, since chemically breaking down the LFP crystal structure is avoided.[8,9]

Here, we report a green and efficient LIB direct recycling strategy based on defect-targeted healing to precisely resolve the Li_v and anti-site defects without altering any other properties of LFP particles. We successfully demonstrate direct regeneration of spent LFP cathodes with various degradation conditions to recover their composition, structure, and electrochemical performance to the same level as that of the pristine LFP cathode. Unlike pyrometallurgical and hydrometallurgical recycling, such defect-targeted direct recycling process only needs a low concentration of lithium salt, green and low-cost reducing agent, nitrogen, and water. With proper modification, this method can also be extended to recycle other "low-cost" LIB cathodes, such as $LiMn_2O_4$ (LMO) batteries. Life-cycle analysis (LCA) of direct recycling of LFP shows that our approach can significantly reduce the energy usage (by ~80%–90%) and GHG emissions (by ~75%), leading to more economic and environmental benefits than the current state-of-the-art approaches.

RESULTS

Low-Temperature Aqueous Relithiation

To demonstrate our defect-targeted direct recycling method, commercial LFP cells were cycled for up to 6,500 cycles in the 2.5–3.8 V voltage range to reach a capacity decay of up to 50% (Figure S1). The cells were disassembled and LFP powders were harvested from the cathodes following the procedures described in our earlier work (details can be seen in Experimental Procedures).[9] The collected cycled LFP particles (denoted as "C-LFP") were subject to relithiation treatment in a Li-containing aqueous solution with controlled temperature and time. The relithiated LFP powders (R-LFP) were washed thoroughly using deionized (DI) water, dried, and then subjected to post-annealing to complete the entire regeneration process (Figure S2).

[1]Department of NanoEngineering, University of California, San Diego, La Jolla, CA 92093, USA

[2]Energy Systems Division, Argonne National Laboratory, 9700 South Cass Avenue, Lemont, IL 60439, USA

[3]Program of Materials Science, University of California, San Diego, La Jolla, CA 92093, USA

[4]Neutron Scattering Division, Oak Ridge National Laboratory, Oak Ridge, TN 37830, USA

[5]Sustainable Power and Energy Center, University of California, San Diego, La Jolla, CA 92093, USA

[6]Program of Chemical Engineering, University of California, San Diego, La Jolla, CA 92093, USA

[7]Department of Chemical and Environmental Engineering, University of California, Riverside, Riverside, CA 92521, USA

[8]Applied Materials Division, Argonne National Laboratory, 9700 South Cass Avenue, Lemont, IL 60439, USA

[9]Chemical Sciences and Engineering Division, Argonne National Laboratory, 9700 South Cass Avenue, Lemont, IL 60439, USA

[10]Lead Contact

*Correspondence: zhengchen@eng.ucsd.edu

https://doi.org/10.1016/j.joule.2020.10.008

Please cite this article in press as: Xu et al., Efficient Direct Recycling of Lithium-Ion Battery Cathodes by Targeted Healing, Joule (2020), https://doi.org/10.1016/j.joule.2020.10.008

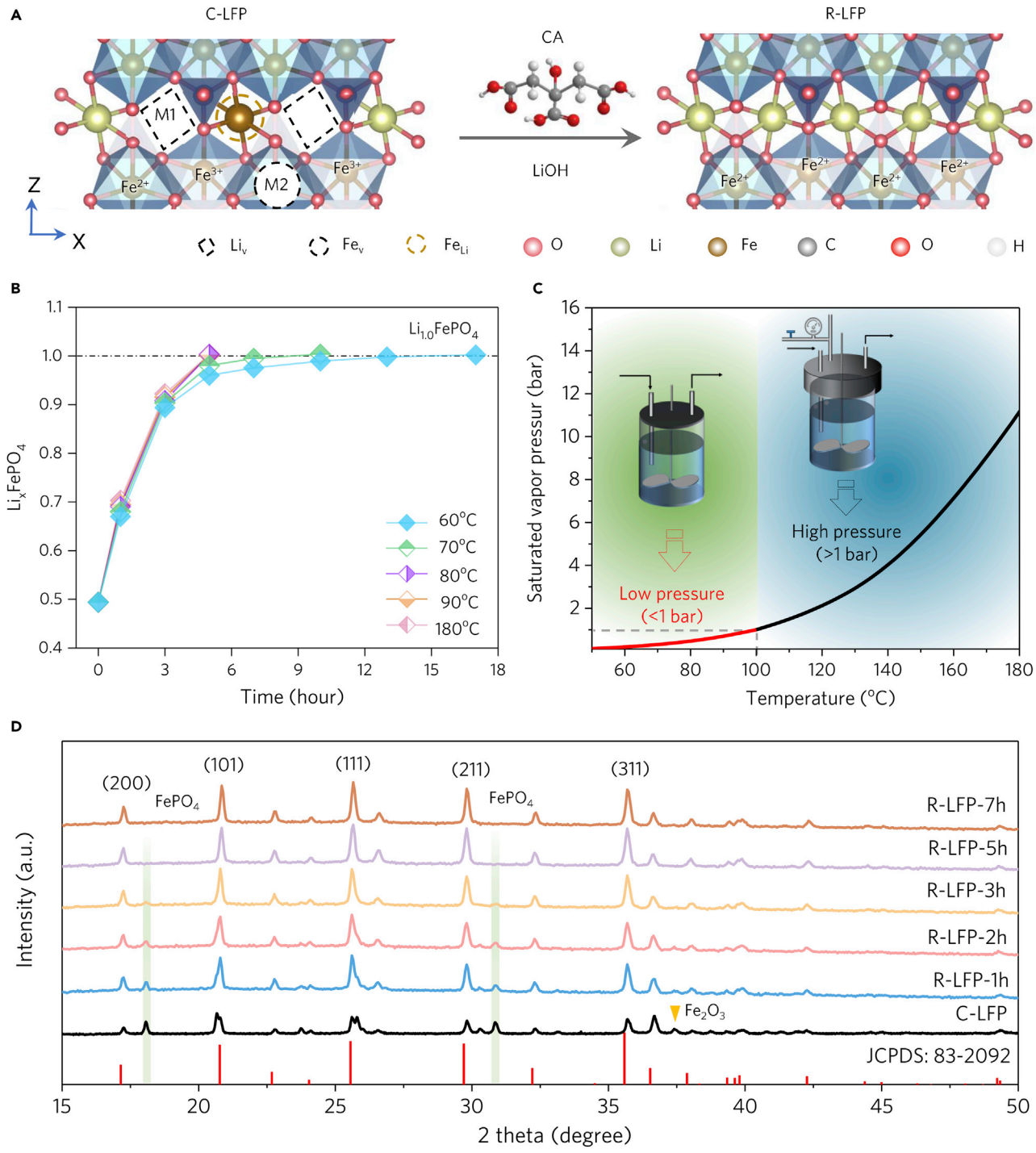

Figure 1. Relithiation Kinetics of C-LFP

(A) Schematic illustration of the solution relithiation process. The positions of Li and Fe in a perfect olivine structure are defined as M1 and M2 sites, respectively. Left side shows C-LFP with Li vacancies (Li_v) and Fe occupation in Li site (Fe_{Li}); right side shows R-LFP with all the Fe^{3+} being reduced to Fe^{2+} with the presence of CA in a LiOH solution.

(B) The evolution of LFP composition during relithiation at different temperatures.

(C) The saturation vapor pressure of water under various temperatures associated with an equipment (schematic) of choice for high pressure (>1 bar) and low-pressure (<1 bar). Effective relithiation at sub-boiling temperature allows pressurized reactors to be replaced by low-cost vessels without extra safety precautions.

(D) XRD patterns of C-LFP and R-LFP with different relithiation time. The gradual diminishment of $FePO_4$ peaks (marked in green) shows the conversion of the $FePO_4$ phase to LFP phase.

Please cite this article in press as: Xu et al., Efficient Direct Recycling of Lithium-Ion Battery Cathodes by Targeted Healing, Joule (2020), https://doi.org/10.1016/j.joule.2020.10.008

As mentioned earlier, the key to regenerate C-LPF is to precisely resolve the Li_v and anti-site defects. A high activation energy (1.4 eV) is required for Fe ions to migrate back to the original position (M2) because of the strong electrostatic repulsion of high valence state of Fe^{3+} during migration (Figure 1A).[10] Kang et al. demonstrated a successful anti-site re-ordering via deep discharging to 1.5 V (versus Li/Li^+) at an extremely low rate of C/100 (1 C responds to charge or discharge in 1 h).[10] The theoretical study also reveals that a reductive environment can lower the activation barrier, which, in turn, can facilitate Fe migration. Therefore, for effective direct regeneration of C-LFP, the most critical step is to reduce Fe^{3+} and re-dose lithium ions (Li^+) into C-LFP.

The half electrode potential of LFP electrode is 0.24 V (versus standard hydrogen electrode or SHE) (Equation 1).[6,11]

$$FePO_4 + Li^+ + e^- \rightarrow LiFePO_4 \quad E(FePO_4/LiFePO_4) = 0.24\ V \qquad \text{(Equation 1)}$$

$$1/2C_6H_8O_7 - e^- \rightarrow 1/2C_5H_6O_5 + 1/2CO_2 + H^+ \quad E(C_5H_6O_5/C_6H_8O_7) = -0.34\ V \qquad \text{(Equation 2)}$$

$$FePO_4 + Li^+ + 1/2C_6H_8O_7 \rightarrow LiFePO_4 + 1/2C_5H_6O_5 + 1/2CO_2 + H^+ \qquad \text{(Equation 3)}$$
$$E(FePO_4/C_6H_8O_7) = 0.58\ V$$

A variety of reducing agents may be used to proceed reduction of Fe^{3+}. Nature-derived organic reductants are particularly interesting, as they are safe and environmentally benign. For example, citric acid (CA), concentrated in citrus fruits, has a redox potential of ~ -0.34 V (versus SHE) (Equation 2), which can be an ideal candidate to assist the reduction of C-LFP.[12,13] The Gibbs free energy for Equation 3, the complete reaction by combining (1) and (2), is calculated to be -56.35 kJ/mol according to Equation 6, indicating that the relithiation reaction of degraded LFP is thermodynamically favorable. In our experiment design, CA in the Li-containing aqueous solution donates electrons to reduce Fe^{3+}, reducing electrostatic repulsion and subsequently lowering the migration barrier to move Fe^{2+} from the M1 site back to the M2 site, which facilitates the solution Li^+ diffusion into the Li-deficient C-LFP particles.

The evolution of LFP composition during the solution relithiation was monitored by inductively coupled plasma mass spectrometry (ICP-MS). We first tested relithiation at 180°C, which is the minimum temperature required for relithiation of degraded layered oxides, such as $LiCoO_2$ and $LiNi_{1-x-y}Co_xMn_yO_2$ cathodes.[8,9,14] As shown in Figure 1B, the Li composition of the C-LFP particles increased from 0.5 to 1.0 as the relithiation time prolonged to 5 h. Note that an autoclave reactor that can hold pressure greater than 11 bar (saturation pressure of water) is typically needed for this operation (Figure 1C).[15] Composition analysis of the relithiation solution before and after reaction showed that 1.9 mol % of Fe was leached from the initial LFP. It might be attributed to the trace amount of Fe_2O_3 generated in the degraded LFP after long-term cycling (Figure 1D).[16,17] From the quality control point of view, leaching the residual Fe_2O_3 phase might be desired as it provides a high-purity LFP phase in the regenerated product.

With the aim to minimize the energy consumption, lower temperatures were explored. Surprisingly, reducing the solution temperature to as low as 80°C resulted in a negligible change in the relithiation kinetics (Figure 1B). Further extending the treatment time allowed a continuous decrease in the solution temperature for relithiation. For example, a 100% composition recovery could be achieved at

temperatures of 70°C and 60°C after 10 and 17 h of relithiation, respectively. The electrochemical impedance spectroscopy (EIS) measurement showed a Li^+ apparent diffusion coefficient ($D_{Li^+}^{app}$) of 1.05×10^{-15} cm^2 s^{-1} for $Li_{0.5}FePO_4$, which is consistent with previous reports.[18] Assuming an average LFP particle size of 100 nm and using the above D_{Li+}, the calculated Li^+ diffusion time matches well with the relithiation time in our experiment (Figure S4), demonstrating that solution relithiation kinetics generally follow the semi-infinite solid-state diffusion mechanism.[19] The effective relithiation at temperatures below the boiling point of water allows the process to be conducted at ambient pressure. Therefore, pressurized reactors can be replaced by low-cost vessels that do not require extra safety precautions, bringing the process one step closer for large-scale operation (Figure 1C).

To further validate the critical role of CA, the same C-LFP was treated with a LiOH solution without CA. As expected, continuous oxidation of ($LiFePO_4$) to Fe_2O_3 and Fe_3O_4 was observed (Figure S5). This result also confirms the effectiveness of defect-targeted healing enabled by CA. In addition, CA is a widely used low-cost (~0.55 $/kg) additive in food industry,[20] and it only generates CO_2, H_2O, and acetonedicarboxylic acid ($C_5H_6O_5$, ~10 $/kg)[21] during the relithiation process. It should be also noted that $C_5H_6O_5$, an important intermediate for drug synthesis, is traditionally prepared by decarbonylation of CA in fuming sulfuric acid.[22] This suggests that our direct LFP recycling process may be coupled with suitable precursors to offer an alternative route for green synthesis of valuable organic molecules. Other reducing agents, such as ascorbic acid (E = -0.55 V),[23] have also demonstrated a similar functionality in regenerating C-LFP (Figure S6), offering a diverse choice of low-cost reducing agents.

X-ray diffraction (XRD) patterns of the C-LFP and samples after solution relithiation for different durations (denoted as "R-LFP") further illustrate the phase transition of degraded LFP during the solution relithiation process (Figure 1D). For example, the C-LFP showed intense peaks at 18° and 32°, which are attributed to the existence of the $FePO_4$ phase due to lithium loss. As the relithiation time increased from 1 to 5 h at a temperature of 80°C, the intensities of these peaks gradually diminished and then disappeared, suggesting the conversion of the $FePO_4$ phase to the LFP phase.

Microstructure Characterization

High-angle annular dark-field (HAADF) scanning transmission electron microscopic (STEM) images were obtained to further understand the relithiation mechanism at the atomic level. For LFP cathode, after over 6,500 cycles, the particles still showed well-defined crystallinity with the carbon coating (2–3 nm) retained on the surface (Figure 2A). The electron energy loss spectroscopy (EELS) experiment was carried out to probe the valence states of O and Fe from the surface to the inner side of the particles (Figure 2B). From one representative particle, the O K-edge and Fe L-edge spectra from the surface (point 1) to the inner side (point 6) of the C-LFP particle were compared. For the C-LFP, the O pre-peak gradually emerged from the surface to the bulk (Figure S7A), suggesting the presence of the Fe^{3+} inside the C-LFP particle.[24] The Fe L-edge gradually shifted from 707.93 to 709.65 eV (Figure 2C; Table S1), suggesting the dominant presence of Fe^{3+} in the bulk.[25] EELS spectra taken from another representative particle are shown in Figure S8. A clear O K-edge pre-peak showed up in the spectrum obtained from the particle surface, indicating the presence of Fe^{3+} on the surface. The above EELS results demonstrate the coexistence of $FePO_4$ and $LiFePO_4$ phases and their random distribution in different particles. Although several two-phase models have been proposed to understand the local structure of delithiated LFP, including the shrinking-core model,[15] mosaic

Please cite this article in press as: Xu et al., Efficient Direct Recycling of Lithium-Ion Battery Cathodes by Targeted Healing, Joule (2020), https://doi.org/10.1016/j.joule.2020.10.008

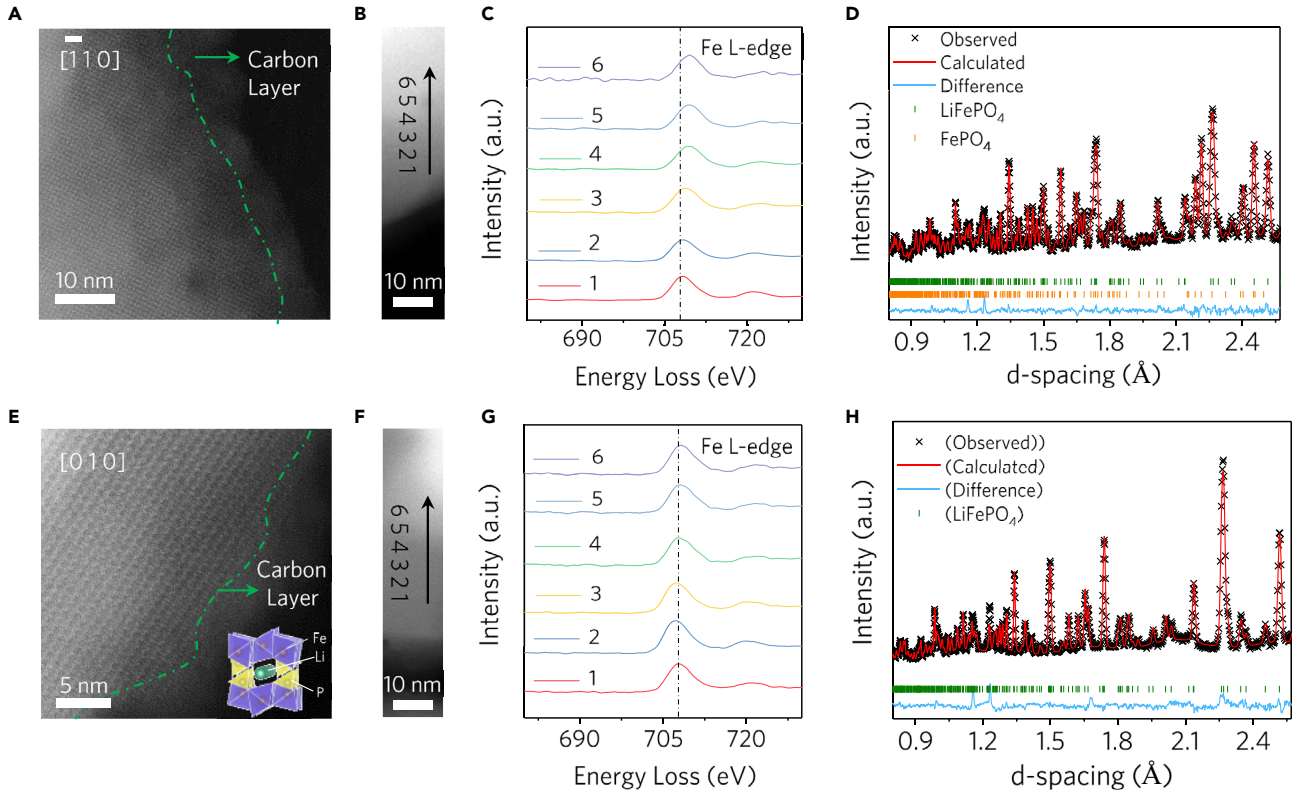

Figure 2. Microstructure Characterization of Different LFP Particles

(A) STEM image of C-LFP. Well-defined orthorhombic crystals with a conformal carbon shell was maintained. The scale bar is 10 nm.

(B) STEM image of a C-LFP particle. The scale bar is 10 nm. Point 1 indicates the surface of the particle and point 6 indicates the inner side of the particle.

(C) Fe L-edge EELS spectra of a C-LFP particle from the surface (point 1) to the bulk (point 6).

(D) Rietveld refinement pattern of the neutron diffraction data of C-LFP.

(E) STEM image of a representative R-LFP particle. The scale bar is 5 nm. Continuous Li^+ diffusion channels along the [010] direction was shown. The carbon shell was maintained after solution relithiation.

(F) STEM image of a representative R-LFP particle. Point 1 and point 6 indicate the surface and the inner side of the particle respectively. The scale bar is 10 nm.

(G) Fe L-edge EELS spectra of a representative R-LFP particle from the surface to the bulk. The unchanged Fe L-edge at 707 eV verifies that the oxidation state of Fe is 2+ from the surface to the bulk.

(H) Rietveld refinement of the neutron diffraction pattern of R-LFP. A pure LFP phase was obtained after the relithiation treatment.

model,[26] and domino-cascade model,[27] they are mainly established upon the first charge and discharge cycles. Our results suggest a high inhomogeneity of phase distributions for the LFP particles after long-term charge/discharge cycles.

Figure 2D depicts the Rietveld refinement pattern of the neutron diffraction data of the C-LFP with the detailed structural information listed in Table S2. Overall, the C-LFP exhibits 47.1% of Li deficiencies (loss) and 4.81% Fe/Li anti-site defects. The computational study by Malik et al. showed that 0.1% anti-site can cause ~5% of Li^+ to be trapped in the defects in a 100 nm $LiFePO_4$ particle.[28] Generally, the Li inventory loss is considered as the main reason for the capacity degradation of LFP batteries,[29,30] while the impact of anti-site defects are often overlooked. Olivine LFP has a *Pnma* space group with Li^+ confined in channels propped up by the interconnecting FeO_6 octahedra and PO_4 tetrahedra. Since the [010] direction is the exclusive pathway for Li^+ diffusion,[10] such a significant occupation of Fe^{2+} in Li sites can block Li^+ diffusion, which leads to loss of capacity and rate performance.

For the R-LFP sample, all the Fe^{2+} around the Li^+ showed ordered structure along the [010] direction, as revealed by the HAADF-STEM image (Figure 2E). The carbon shell was also retained after solution relithiation. The disappearance of the O pre-peak (Figure S7B) and the unchanged Fe L-edge at 707 eV (Figure 2F) verified that the oxidation state of Fe from the surface to the bulk remained as 2+.[24] The neutron diffraction data (Figure 2G) further confirm that a pure orthorhombic LFP phase was obtained after the relithiation treatment, with the ratio of anti-site defects reduced to as low as 2.2% (Table S3), which is even lower than the pristine LFP (denoted as "P-LFP") (2.5%).

High crystallinity LFP (denoted as "RA-LFP") with further reduced anti-site defects were obtained after a short annealing treatment of the R-LFP. The XRD patterns for each sample were examined to identify possible structural changes (Figure S9). While the average grain size grew from 72 to 96 nm (Figure S10) as the annealing temperature increased from 400 to 800°C, no phase changes were observed. A uniform carbon coating also remained on the particle surface, as shown by the homogeneous distribution of C, P, and Fe elements in element mapping (Figure S11), further suggesting the targeted healing of the composition and microstructure defects in C-LFP.

Operando neutron diffraction was performed to quantify the evolution of Fe_{Li} anti-site defects during annealing. The time-dependent contour plot of peak intensity (Figure 3A) further confirmed that pure LFP phase was maintained during heating and cooling, demonstrating good stability of the R-LFP particles. After cooling down, the ratio of anti-site defects was reduced to 1.5% (Figures 3B and S12A; Table S4), which was further reduced compared with that of the P-LFP (2.5%) (Figure S12B; Table S5). In contrast, significant phase impurities (e.g., Li_3PO_4, Fe_2P) always existed after the solid-state reaction-based regeneration process (SS), where Li-containing precursor (e.g., Li_2CO_3, LiOH) was mixed with degraded LFP particles for annealing (Figure S13). It is a clear advantage that the solution-based relithiation ensures homogeneous Li distribution inside LFP particles, which eliminates phase impurities after annealing.

Electrochemical Performance Evaluation

The electrochemical performance of LFP samples was first evaluated using half cells. The cycling test started with 0.1 C (1 C = 170 mA g^{-1}) activation for 2 cycles followed by 0.5 C for another 100 cycles (Figure 3C). The P-LFP showed a capacity of 161 mAh g^{-1} at 0.5 C with a negligible capacity decay after 100 cycles. The capacity of the C-LFP recovered from spent cells was only 103 mAh g^{-1} at 0.5 C, which further decreased to 98 mAh g^{-1} after 100 cycles. The initial capacity of the R-LFP was dramatically improved to 159 mAh g^{-1}, indicating the restored electrochemical activity after solution relithiation. However, only 93.7% of the initial capacity was maintained after 100 cycles. Such a degradation is probably associated with the Li^+/proton exchange during the aqueous relithiation, which has a negligible effect on the crystal structure,[31] but induced side reactions due to the existence of protons. The following short annealing step helped to create more stable particles that could deliver the same capacity and stability as that of the P-LFP. It was found that too low temperatures might aggravate structure defects, as shown in the previous study of LFP synthesis,[32,33] and too high temperatures lead to a larger grain size. Both cases led to an inferior capacity of RA-LFP to P-LFP (Figure S14). Thermal annealing at 600°C for 2 h enabled RA-LFP to deliver a capacity of 159 mAh g^{-1} at 0.5 C with less than 1% of capacity loss after 100 cycles. With an extended cycling at 0.5 C for 1,000 cycles, the RA-LFP could still deliver a capacity of 150 mAh/g (Figure S15).

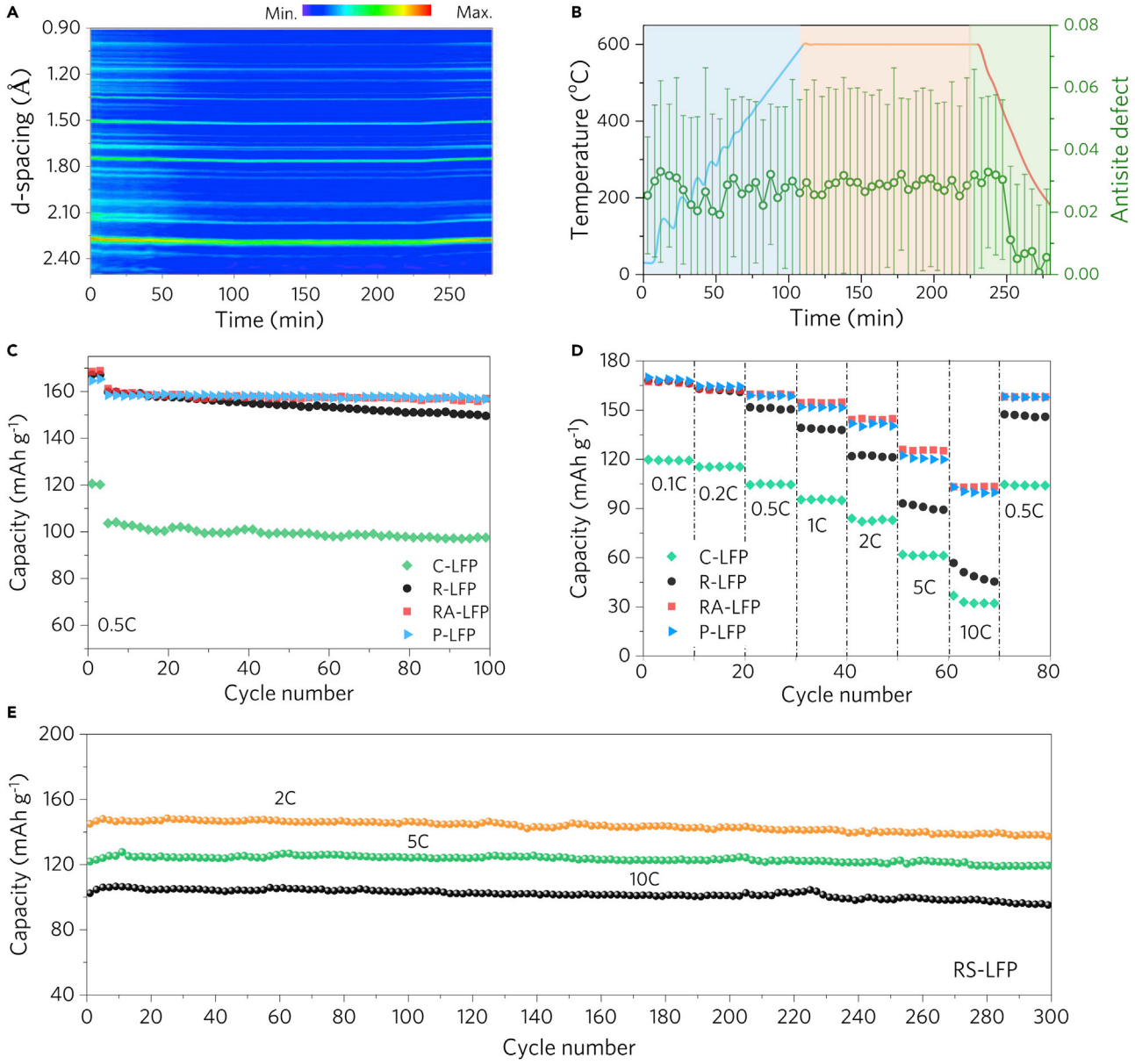

Figure 3. Electrochemical Performance of LFP Electrodes

(A) Time-dependent contour plot of diffraction peak intensity in the heating, holding and cooling stages. The blue and red color represent the minimum and maximum intensity of peaks.

(B) Anti-site defects revolution upon heating (blue line), holding (orange line) and cooling (red line). The dots with error bars correspond to the ratio of the anti-site defects.

(C) Cycling stability of C-LFP, R-LFP, RA-LFP and P-LFP. Electrodes were cycled at 0.1 C for activation and 0.5 C for the following cycles.

(D) Rate performance of C-LFP, R-LFP, RA-LFP, and P-LFP.

(E) Long-term cycling stability of RA-LFP cycled at 2 C, 5 C, and 10 C for 300 cycles.

The rate capability of the C-LFP could also be recovered after the complete regeneration (Figure 3D). Specifically, the P-LFP could deliver a capacity of 163, 141, and 99 mAh g^{-1} at 0.2, 2, and 10 C, respectively. The capacity of RA-LFP increased to 162, 144, and 102 mAh g^{-1}, superior to that of P-LFP, especially at high rates. In contrast, the C-LFP could only provide a capacity of 115, 82, and 66 mAh g^{-1}, due to the Li loss and structure defects. Moreover, the regenerated LFP also

Please cite this article in press as: Xu et al., Efficient Direct Recycling of Lithium-Ion Battery Cathodes by Targeted Healing, Joule (2020), https://doi.org/10.1016/j.joule.2020.10.008

exhibited excellent long-term cycling stability. No obvious capacity loss was observed after 300 cycles at 2 C, 5 C, and 10 C rates (Figure 3E). The significantly improved rate performance and high stability of the RA-LFP suggest that both the composition and structure of C-LFP have been completely recovered after the relithiation and short annealing treatment.

In general, a 20% capacity loss is considered to be the end of life for EVs batteries.[34] By considering secondary use, one can assume that 50% capacity decay might be the lower limit of the service life of an LIB for any applications.[35] In reality, an LIB waste stream might consist of cells with various degradation conditions. Therefore, we tested our method on a mixture of cycled cathode materials with states of health (SOH) of 40%, 50%, and 85% (Figure S16) to fully examine the effectiveness of our process. Subjected to the same regeneration process as described earlier, the cycled LFP mixture showed a complete recovery of composition, structure, and electrochemical performance to the same level as that of the P-LFP (Figures S16A–S16C). This result suggests significant advantages of using the low-temperature solution relithiation method to treat spent batteries with a diverse range of health conditions, as all the cathodes reach a stoichiometric composition due to self-saturation (Figure S16D).

In order to further examine the practical application of the fully regenerated LFP (RA-LFP), commercially relevant thick electrodes with a mass loading of ~19 mg/cm^2 were prepared, which were used to assemble both half cells (with Li metal as the counter electrode) and pouch cells (with graphite as the anode). The corresponding electrochemical performance is shown in Figure S17. The high-loading half cells showed an initial capacity of 156 mAh/g and maintained at 155 mAh/g after 100 cycles at 0.5 C. The pouch cell (3 cm × 3 cm) could deliver a capacity of 28.6 mAh (3.17 mAh/cm2 and 167 mAh/g) at the rate of 0.1 C and showed no capacity degradation after 100 cycles. These results further suggest the great potential of using directly regenerated LFP to manufacture new cells without sacrificing cell-level performance.

Economic and Environment Analysis

Figure 4A illustrates a brief flowchart of cathode regeneration from direct recycling of cathodes from spent LIB materials, as well as pyrometallurgical recycling, hydrometallurgical recycling, and virgin cathode material production. It should be noted that currently pyrometallurgical and hydrometallurgical recycling routes are not used commercially to recover cathode material from spent LFP batteries due to the economic loss they incur. We include them here as potential end-of-life management options for LFP batteries, assuming that battery recycling is mandated while new recycling technologies are not yet available. Compared with other processes, clear advantages of developing the direct recycling process for LFP lie in: (1) simplified operation facilities and processes, (2) reduced operation temperature and time, and (3) eliminating the usage of strong acid and base. These features are associated with the potential economic and environmental benefits that can be analyzed by the EverBatt model developed by Argonne National Laboratory.[36]

The three different recycling methods are modeled assuming an annual plant processing capacity of 10,000 tons of spent batteries (Figure 4B). The life-cycle total energy use for pyrometallurgical and hydrometallurgical processes are 18.4 and 30.6 MJ kg^{-1} LFP cell, respectively. In the pyrometallurgical process, 55% of the energy use is attributed to high temperature smelting. In the hydrometallurgical process, 87.8% of the energy use comes from upstream production of the chemicals consumed in the process. The total energy use for direct recycling is only

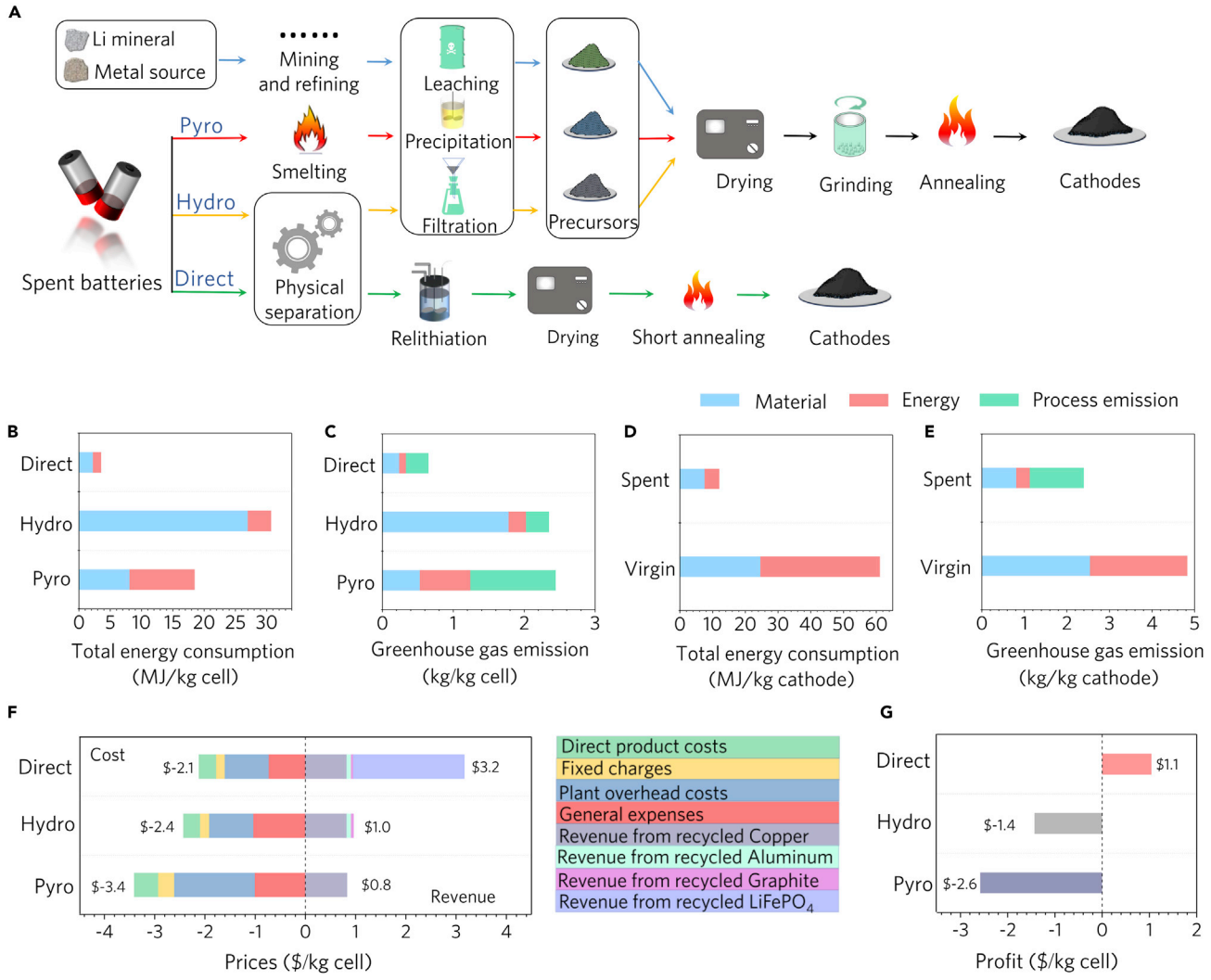

Figure 4. Economic and Environment Analysis

(A) Simplified schematic of pyrometallurgical ("Pyro") and hydrometallurgical ("Hydro") and direct recycling ("Direct") methods, as well as cathode production from virgin materials mining.

(B) Total energy consumption of recycling 1 kg spent cell with pyrometallurgical, hydrometallurgical, and direct technology.

(C) GHG emissions of recycling 1 kg spent cell with pyrometallurgical, hydrometallurgical, and direct technology.

(D) Total energy consumption of manufacturing 1 kg cathode from virgin and recycled materials.

(E) GHG emissions of manufacturing 1 kg cathode from virgin and recycled materials.

(F) Cost and revenue per kg of spent LFP batteries recycled by pyrometallurgical, hydrometallurgical, and direct recycling. Cost: $ -3.4 (Pyro); $ -2.4 (Hydro); $ -2.1 (Direct). Revenue: $ 0.8 (Pyro); $ 1.0 (Hydro); $ 3.2 (Direct).

(G) Profit of recycling 1 kg of spent LFP batteries with pyrometallurgical, hydrometallurgical, and direct technology, respectively. Profit: $ -2.6 (Pyro); $ -1.4 (Hydro); $ -1.1 (Direct).

3.5 MJ kg^{-1} LFP cell, significantly lower than the other processes. GHG emissions are also an important factor to consider when evaluating a recycling approach. As shown in Figure 4C, the total GHG emissions released from the direct recycling process are only 26.6% and 27.7% of those from pyrometallurgical and hydrometallurgical processes, respectively. Moreover, the total energy use per kg of cathode made from direct recycling of the spent batteries is only 22.3% compared with that of the cathode produced from virgin materials (Figure 4D). The GHG emissions from cathode production via direct regeneration of spent batteries is 46.2% lower than that from virgin materials (Figure 4E).

Please cite this article in press as: Xu et al., Efficient Direct Recycling of Lithium-Ion Battery Cathodes by Targeted Healing, Joule (2020), https://doi.org/10.1016/j.joule.2020.10.008

The cost and profit are also modeled, and the results are shown in Figure 4F. The total cost of pyrometallurgical, hydrometallurgical, and direct recycling is $3.4, $2.4, and $2.1 per kg of spent battery cells processed, respectively. It should be noted that any recycled Al, Cu, graphite is assumed to be sold to compensate some cost, but the net revenue cannot cover the high cost of the pyrometallurgical and hydrometallurgical recycling processes, due to the use of expensive equipment and significant quantities of materials, and high energy consumption. This is the main reason why today's industry is not cycling LFP cells.[37] Nevertheless, using direct recycling, the regenerated cathode materials can be readily used by cell manufacturers without further re-synthesis, which results in a potential profit of 1.04 $ per kg of recycled spent batteries (Figure 4G). It should be admitted that the EverBatt model-based LCA offers a guide to the likelihood of commercial viability and is not intended to provide a precise economic judgment for immediate industry implementation without careful examination in a real operation, as the above LFP recycling processes have not been used in a large industry scale.

Because of significant reductions in total energy use and GHG emissions and a lower cost, the low-temperature aqueous relithiation-based direct regeneration method may be a preferable option for spent LIB recycling. Methods for LFP recycling explored so far remain to be based on hydrometallurgical processes or other destructive processes.[38–44] Ideally, solid-state annealing by adding a desired amount of lithium back into spent LFP cathode powders may also restore their original composition. However, it is practically challenging to determine an accurate quantity of lithium dosage for a large number of spent cells having significantly different SOHs. More importantly, defect-targeted healing cannot be achieved as manifested by the relatively low capacity of recycled LFP from solid-state annealing.[45–47] While chemical lithiation in an aprotic solvent (e.g., acetonitrile) using strong reducing agent may also be used to re-functionalize spent LFP,[48] the highly caustic nature of such a system can prohibit its practical application.

Another advantage of using our ambient-condition solution process is that the relithiation solution can be also recycled. For example, the used solution with LiOH and CA was tested to relithiate a second batch of spent LFP under the same condition. The XRD patterns and cycling stability of RA-LFP regenerated with a fresh and recycled solution are compared in Figure S18. A pure LFP phase can be obtained even with the recycled solution of LiOH and CA. The capacity and stability of RA-LFP produced from the recycled relithiation solution reached the same level as the LFP regenerated with a fresh solution of LiOH and CA. The successful demonstration of recycling and reuse of relithation solution of LiOH and CA can provide the possibility to further reduce the overall operation cost of our direct recycling method.

DISCUSSION

Here, we have demonstrated a defect-targeted healing method to recycle spent LIB materials more efficiently, which could be a paradigm-shift route toward potentially profitable and green recycling of LIBs that are not viable for today's recycling processes. A complete recovery of the electrochemical performance of spent LFP cathodes to the level of their pristine counterparts can improve the market acceptance of recycled battery materials. Moreover, LCA by assuming 10,000 tons of annual plant processing capacity of spent batteries suggests that our direct regeneration route has low energy consumption of 3.5 MJ kg^{-1} LFP cell (accounting for only 19% and 11% of pyro- and hydrometallurgical processes, respectively) and low GHG emissions of 0.7 kg/kg LFP cell (26.6% and 27.7% of pyro- and hydrometallurgical

Please cite this article in press as: Xu et al., Efficient Direct Recycling of Lithium-Ion Battery Cathodes by Targeted Healing, Joule (2020), https://doi.org/10.1016/j.joule.2020.10.008

processes, respectively). More importantly, the cost of direct regeneration can be reduced to $2.1 per kg spent LFP cell, which is $3.4 and $2.4 for pyro- and hydrometallurgical processes, respectively. It should be noted that even though there are uncertainties of the costs from battery collection and transportation, they are considered to be the same, regardless of recycling processes if they are collected from the same source. Thus, the reduced cost from direct recycling is mainly due to the significantly improved operation design and less chemical usage in the processing. Further study to improve the logistics in transportation, battery handling, and materials separation will help to close the loop for this direct recycling method, which will pave the way for its industrial adoption.

EXPERIMENTAL PROCEDURES

Resource Availability

Lead Contact

Further information and requests for resources and reagents should be directed to and will be fulfilled by the Lead Contact, Zheng Chen (zhengchen@eng.ucsd.edu).

Materials Availability

This study did not generate new unique reagents.

Data and Code Availability

The datasets generated in this study are available from the Lead Contact on request.

$LiFePO_4$ Cell Cycling and Cathode Materials Harvesting

Commercial LFP cells (Tenergy, 2,500 mAh) were cycled in the voltage range of 2.5–3.8 V using an Arbin battery tester for over 6,500 cycles and then discharged to 2 V at C/10 (1 C=170 mA g^{-1}) before disassembly. The cathode strips were thoroughly rinsed with dimethyl carbonate (DMC) to remove residual electrolyte. After drying, the cathode strips were soaked in N-Methyl-2-pyrrolidone (NMP) for 30 min followed by sonication for 20 min, which removed the LFP powders, binder, and carbon black from the aluminum substrates. The obtained suspension was centrifuged at 3,500 rpm for 5 min and the cycled LFP (C-LFP) powders were precipitated, separated, and dried for regeneration. Fresh cells were directly discharged to 2 V at C/10 without any cycling before disassembly, and the harvested LFP material served as the reference material for comparison. The schematic illustration of the materials harvesting process is shown in Figure S2.

$LiFePO_4$ Regeneration

The C-LFP was regenerated through a solution relithiation followed by a short annealing process. For the solution relithiation treatment, LFP powders harvested from the cycled cells were loaded into a 100 mL reactor filled with 80 mL of 0.2 M LiOH and 0.08 M CA solutions. The reactor was kept at a wide range of temperatures for various operation times for relithiation. The relithiated LFP (R-LFP) powders were washed thoroughly with deionized water, and dried. The R-LFP was then mixed with excess 4% Li_2CO_3 and subject to thermal annealing at different temperatures for 2 h in nitrogen with a temperature ramping rate of 5°C min^{-1}. The final recycled LFP is denoted as RA-LFP.

Characterization of Regenerated $LiFePO_4$

The crystal structure of the powders was examined by XRD employing Cu Kα radiation. The X-ray photoelectron spectroscopy (XPS) measurement was performed with Kratos AXIS Ultra DLD with Al Kα radiation. The composition of pristine, degraded, and regenerated LFP cathode was measured by an inductively coupled plasma mass

spectrometry (ICP-MS). HRTEM was recorded on JEOL-2800 at 200 kV with Gatan OneView Camera. STEM-EDS was performed on primary particles a at annular dark-field (ADF) mode using the same instrument. STEM-EELS was performed on JEOL JEM-ARM300CF at 300 kV, equipped with double correctors. *Ex situ* neutron diffraction patterns were collected in the high-resolution mode ($\Delta d/d \sim 0.25\%$) for a duration of 2 h under the nominal 1.1 MW SNS operation, and then processed using VDRIVE software.[49] *Operando* neutron diffraction data were collected in the high intensity mode ($\Delta d/d \sim 0.45\%$), while the powders were heated and cooled in a furnace under nitrogen atmosphere.[21,50]

Electrochemical Characterization

To evaluate electrochemical performance using electrodes with moderate mass loading, different LFP powder samples were mixed with polyvinylidene fluoride (PVDF) and Super P65 in NMP at a mass ratio of 8:1:1. The resulted slurries were cast on aluminum foils, followed by vacuum drying at 120°C for 6 h. Circle-shaped electrodes were cut and compressed, with controlled active mass loading of about 3–5 mg cm^{-2}. To make electrodes for high-mass loading half-cell and pouch full-cell testing, the cathode casting was made with a commercial relevant ratio (RA-LFP: Super P: PVDF = 95:2:3) and the mass loading of active material was controlled at ~19 mg/cm^2. Galvanostatic charge-discharge was carried out in the potential range of 2.5–3.8 V with the assembled cells. The electrolyte was LP40 (1 M $LiPF_6$ in ethylene carbonate/diethyl carbonate = 50:50 (v/v)). The cells were cycled with activation for 3 cycles at 0.1 C followed by extended cycling at higher rates. The EIS tests were performed at discharged state in the frequency range of 10^6 Hz to 10^{-3} Hz with signal amplitude of 10 mV by a Metrohm Autolab potentiostat.

Calculation of Gibbs Free Energy

The $E(FePO_4/LiFePO_4)$ = 0 + 0.24 V = 0.24 V (versus SHE) is obtained from the reductive peak of the CV curve, which is shown in Figure S3.

The CV was tested in 3-electrode configuration with C-LFP as the working electrode, Pt as the counter electrode and saturated calomel electrode (SCE) as the reference electrode. Notably, the electrolyte was exactly same as the relithiation solution, which can be used to accurately identify the lithiation potential of LFP.

$$1/2C_6H_8O_7 - e^- \rightarrow 1/2C_5H_6O_5 + 1/2CO_2 + H^+ \quad \text{(Equation 4)}$$

$E(C_5H_6O_5/C_6H_8O_7)$ = -0.34 V (versus SHE) was calculated based on the Nernst equation, where E^{Θ} is obtained from literature (−0.18 V),[51] n is the number of moles of electrons, R is the gas constant, and T is temperature in Kelvin.

$$E = E^{\theta} - \left(\frac{RT}{ZF}\right) \times ln\left(\frac{C_{red}}{C_{ox}}\right) \quad \text{(Equation 5)}$$

$$= E^{\theta} - \left(\frac{RT}{ZF}\right) \times \ln\left(\frac{C_{(C_6H_8O_7)}}{C_{(C_6H_8O_7)} \times P_{CO_2} \times C^2_{H^+}}\right)$$

where the pH value (5.38) was obtained from pH meter. Besides, only the effect of pH value was considered here. The activities of other species were set as 1. The Gibbs free energy for the complete reaction (Equation 3 in the main text) can be calculated using the following equation:

$$\Delta G = -nFE \quad \text{(Equation 6)}$$

$$= -nF(E(FePO_4/LiFePO_4) - E(C_5H_6O_5/C_6H_8O_7))$$

Please cite this article in press as: Xu et al., Efficient Direct Recycling of Lithium-Ion Battery Cathodes by Targeted Healing, Joule (2020), https://doi.org/10.1016/j.joule.2020.10.008

Calculation of Diffusion Time of Li^+ into the Crystal Structure

The Li^+ apparent diffusion coefficient and time at different temperatures were calculated. The details of the calculation are shown as follows:

$$D_{Li^+}^{app} = \frac{R^2T^2}{2A^2n^4F^4C^2\sigma^2} \quad \text{(Equation 7)}$$

where R is the gas constant, T the absolute temperature, A the interface between the cathode and electrolyte (A =1.6 cm^2), n the number of electrons involved in the reaction, F the Faraday constant, C the concentration of Li^+ in the electrode (= ρ/M) based on the molecular weight of LFP (M) and density (ρ), and σ the Warburg factor. The Warburg factor can be obtained from the slope of Z' versus $\omega^{-1/2}$ plots (ω is the angular frequency) in the Warburg region. The results of the Z' versus $\omega^{-1/2}$ for the C-LFP, along with the linear fitting curves, are shown in Figure S4B.

$$Z_{real} = \sigma\,\omega^{-1/2} \quad \text{(Equation 8)}$$

Based on the obtained slope, the Li^+ apparent diffusion coefficient for the LFP sample was calculated to be 1.05×10^{-15} cm^2/s.

The apparent diffusion coefficient in solids at different temperatures can be predicted by the Arrhenius equation.

$$D_{Li^+}^{app} = D_0 e^{-E_a/kT} \quad \text{(Equation 9)}$$

where $D_{Li^+}^{app}$ is the lithium apparent diffusion coefficient, E_a the activation energy (3.1eV),[52] k the Boltzmann constant (8.617×10^{-5} eV/K), and D_0 the pre-exponential factor.

The relation between the mean diffusion time of Li^+ and the $D_{Li^+}^{app}$ diffusion coefficient can be estimated with the following the equation:

$$t = \frac{R^2}{4D_{Li^+}^{app}} \quad \text{(Equation 10)}$$

where t is the Li^+ diffusion time, $D_{Li^+}^{app}$ the diffusion coefficient at different temperature, and R the diffusion length (~100 nm). The calculated diffusion time as a function of temperature was plotted, as shown in Figure S4C.

Economic and Environmental Analysis

The EverBatt model, a closed-loop battery recycling model developed at Argonne National Laboratory,[36] was used to conduct techno-economic and life-cycle analysis of pyrometallurgical, hydrometallurgical, and direct cathode recycling processes. The cathode production from virgin materials was also modeled for comparison. Our analysis was focused on the total energy use and GHG emissions of the three recycling methods and did not include the emissions or energy associated with their use in electric vehicles. Moreover, the cost and revenue of the three recycling methods were modeled as well.

Evaluation of the Life-Cycle Total Energy Use and Greenhouse Gas (GHG) Emissions in Recycling

Pyrometallurgical (Figure S19) and hydrometallurgical (Figure S20) recycling processes were included as battery end-of-life management options. Although one could argue that the entire process may not be applicable to the recycling of LFP batteries, especially the steps focusing on Ni and Co recovery (e.g., leaching, solvent extraction, precipitation), in the current recycling industry, pyrometallurgical and hydrometallurgical recyclers do not sort batteries before processing. As a result,

Please cite this article in press as: Xu et al., Efficient Direct Recycling of Lithium-Ion Battery Cathodes by Targeted Healing, Joule (2020), https://doi.org/10.1016/j.joule.2020.10.008

spent batteries will end up going through the same recycling process regardless of cathode chemistry, as assumed in this study.

The generic direct recycling process in EverBatt was modified in this study to reflect the changes in the process design, as depicted in Figure S21. In the direct recycling process, batteries are discharged, dissembled, and shredded. After that, the materials undergo a series of physical separation processes to separate out scrap metals, plastics, anode powder and cathode powder. After separation, the harvested cathode materials are sent to relithiation and thermal annealing to produce rejuvenated cathode powder. The three recycling plants, featuring pyrometallurgical, hydrometallurgical, and direct recycling processes, respectively, are assumed to be based on processing 10,000 metric tons of battery cells per year in the US. The modeling of the life-cycle total energy and GHG emissions was based on the materials and energy flows through the recycling process, as discussed below.

Materials Input

The materials requirements for the three recycling technologies are summarized in Table S6. The materials requirements for the generic pyrometallurgical and hydrometallurgical processes are obtained from EverBatt and are reproduced here for the readers' understanding. The materials requirements for the direct recycling process are obtained based on our lab process. The life-cycle analysis accounts for the environmental impacts of all the materials consumed in the process(es) by capturing the environmental impacts associated with their upstream production.

Energy Input

To calculate the life-cycle environmental impacts attributable to all types of energy consumed in the process(es), the life-cycle analysis considers the environmental impacts associated with upstream fuel production and electricity generation, as well as those associated with on-site fuel combustion (e.g., diesel/natural gas combustion). The energy requirements to recycle 1 kg of spent batteries through different recycling technologies are summarized in Table S7. Again, the purchased energy consumptions for the generic pyrometallurgical and hydrometallurgical processes are obtained from EverBatt, while that for the direct recycling process is estimated from engineering calculations based on our lab process.

Process Emissions

In the life-cycle analysis, we also accounted for environmental impacts associated with process emissions that are not due to fuel combustion. For the three recycling processes, process emissions include those from material combustion and thermal decomposition. The former arises from burning off materials during the recycling processes, including graphite, carbon black, electrolyte, plastics, and the binder material in the pyrometallurgical process, and electrolyte and the binder material in the hydrometallurgical and direct recycling processes. The latter arises from the decomposition of Li_2CO_3 during the relithiation step of the direct recycling process. As the pyrometallurgical process involves burning off various battery constituents, it leads to much higher emissions than those from the other two recycling methods. The detailed modeling results are listed in Table S8. The total energy use and GHG emissions are plotted as column chart shown in Figure 4B. Total energy use is the cumulative energy use pertaining to the process, including fossil energy use and renewable energy use. Fossil energy use can be further broken down to that of coal, natural gas, and petroleum. GHG emissions are calculated based on a 100-year global warming potential data from the fifth assessment report of the intergovernmental panel on climate change.[53]

Energy Consumption and Emissions Evaluation from Cathode Production

The scheme of cathode production from virgin materials and cathode regeneration from spent batteries are shown in Figure 4A. When comparing the results of regenerated LFP with virgin LFP, it is important that all spent batteries handling steps beyond recycling are also considered. In this study, we accounted for spent battery collection and transportation as well, with assumed transportation distances of 50 and 1,000 miles, respectively. Since 0.294 kg of LFP can be regenerated from direct recycling of 1 kg of spent LFP batteries, the environmental impacts for 1 kg of regenerated LFP are calculated and listed in Table S9, together with those for 1 kg of virgin LFP, which are from EverBatt. The modeled energy consumption and emissions are shown in Table S9, which are plotted in Figures 4D and 4E.

Cost and Revenue Analysis of Different Recycling Processes

The specific cost parameters chosen for the recycling plant are summarized in Table S10. The revenue calculation was based on the sales of recycled materials. The prices are obtained from EverBatt and listed in Table S11. The recycled yield of components is assumed to be 90%. "NA" means the material cannot be accessible in the specific recycling. The weight percentage of Cu, Al, graphite and LFP in a cell is 13.9%, 7.5%, 16.8%, and 32.7%, respectively. Combining with the cost obtained from Table S10, the achieved profit is calculated and shown in Figure 4G.

SUPPLEMENTAL INFORMATION

Supplemental Information can be found online at https://doi.org/10.1016/j.joule.2020.10.008.

ACKNOWLEDGMENTS

This work was supported by US National Science Foundation via award CBET-1805570 (for experimental work), US Department of Energy via ReCell Center (for EverBatt modeling work), and the start-up fund support from the Jacob School of Engineering at UC San Diego to Z.C.; M.Z. and Y.S.M. acknowledge the funding support from Zable Endowed Chair Fund. We acknowledge the UC Irvine Materials Research Institute for the use of the (S)TEM facilities, funded, in part, by the NSF Major Research Instrumentation Program under grant CHE-1338173. The part of the work at Argonne National Laboratory was supported from the U. S. Department of Energy (DOE), Office of Energy Efficiency and Renewable Energy, Vehicle Technologies Office. Argonne National Laboratory is operated for DOE Office of Science by UChicago Argonne, LLC, under contract number DE-AC02-06CH11357. A portion of the work used the UCSD-MTI Battery Fabrication Facility and the UCSD-Arbin Battery Testing Facility. The neutron diffraction work used resources at the Spallation Neutron Source, a US Department of Energy (DOE) Office of Science User Facility operated by the Oak Ridge National Laboratory. We thank Ms. S.B. for assistance on TEM characterization. The authors also thank Prof. Jeff Dahn at Dalhousie University for comments and suggestions on the experiment and the revision of the manuscript.

AUTHOR CONTRIBUTIONS

Z.C. conceived the idea, designed the experiment, and directed the project. P.X. carried out the synthesis, processing and electrochemical evaluations and analyzed the data. P.X. and Q.D. performed the economic and environmental modeling. H.G. assisted the experiment design and studied the relithiation kinetics. H.L., Y.C., and K.A. assisted with neutron diffraction characterization. M.Z. collected and analyzed the (S)TEM and EELS data. M.L. made the pouch cells. P.X. and Z.C. wrote the

manuscript. Y.S.M., P.L., Y.L., J.S.S., L.G., and J.L. revised the manuscript and interacted with other authors regarding experiment design and data analysis. All the authors discussed the results and commented on the manuscript.

DECLARATION OF INTERESTS

A patent was filed for this work through the UCSD Office of Innovation and Commercialization.

Received: July 15, 2020
Revised: August 24, 2020
Accepted: October 8, 2020
Published: November 12, 2020

REFERENCES

1. Li, J., and Ma, Z. (2019). Past and present of $LiFePO_4$: from fundamental research to industrial applications. Chem *5*, 3–6.
2. Tran, M.K., Rodrigues, M.F., Kato, K., Babu, G., and Ajayan, P.M. (2019). Deep eutectic solvents for cathode recycling of Li-ion batteries. Nat. Energy *4*, 339–345.
3. Ciez, R.E., and Whitacre, J.F. (2019). Examining different recycling processes for lithium-ion batteries. Nat Sustain *2*, 148–156.
4. Lv, W., Wang, Z., Cao, H., Sun, Y., Zhang, Y., and Sun, Z. (2018). A critical review and analysis on the recycling of spent lithium-ion batteries. ACS Sustainable Chem. Eng. *6*, 1504–1521.
5. Pillot, C. (2019). The rechargeable battery market and main trends 2018–2030 Proceedings of the Advanced Automotive Battery Conference.
6. Padhi, A.K., Nanjundaswamy, K.S., Masquelier, C., Okada, S., and Goodenough, J.B. (1997). Effect of structure on the Fe^{3+}/Fe^{2+} redox couple in iron phosphates. J. Electrochem. Soc. *144*, 1609–1613.
7. Islam, M.S., Driscoll, D.J., Fisher, C.A.J., and Slater, P.R. (2005). Atomic-scale investigation of defects, dopants, and lithium transport in the $LiFePO_4$ olivine-type battery material. Chem. Mater. *17*, 5085–5092.
8. Shi, Y., Chen, G., Liu, F., Yue, X., and Chen, Z. (2018). Resolving the compositional and structural defects of degraded $LiNi_xCo_yMn_zO_2$ particles to directly regenerate high-performance lithium-ion battery cathodes. ACS Energy Lett. *3*, 1683–1692.
9. Shi, Y., Chen, G., and Chen, Z. (2018). Effective regeneration of $LiCoO_2$ from spent lithium-ion batteries: A direct approach towards high-performance active particles. Green Chem. *20*, 851–862.
10. Park, K., Park, I., Kim, H., Lim, H., Hong, J., Kim, J., and Kang, K. (2014). Anti-site reordering in $LiFePO_4$: defect annihilation on charge carrier injection. Chem. Mater. *26*, 5345–5351.
11. Wang, L., Zhou, F., Meng, Y.S., and Ceder, G. (2007). First-principles study of surface properties of $LiFePO_4$: surface energy, structure, Wulff shape, and surface redox potential. Phys. Rev. B *76*, 165435.
12. Xue, C., Métraux, G.S., Millstone, J.E., and Mirkin, C.A. (2008). Mechanistic study of photomediated triangular silver nanoprism growth. J Am Chem Soc *130*, 8337–8344.
13. Shatokha, V. (2018). Iron Ores and Iron Oxide Materials (IntechOpen), pp. 165–167. https://www.intechopen.com/books/iron-ores-and-iron-oxide-materials.
14. Sloop, S.E. (2008). Reintroduction of Lithium into Recycled Battery Materials. Patent No. US 8846225B2, filed February 20, 2009, granted September 30, 2014.
15. Yamada, A., Koizumi, H., Sonoyama, N., and Kanno, R. (2005). Phase change in Li_xFePO_4. Electrochem. Solid State Lett. *8*, 409–413.
16. Chen, J., Li, Q., Song, J., Song, D., Zhang, L., and Shi, X. (2016). Environmentally friendly recycling and effective repairing of cathode powders from spent $LiFePO_4$ batteries. Green Chem. *18*, 2500–2506.
17. Song, L., Li, X., Wang, Z., Xiong, X., Xiao, Z., and Zhang, F. (2012). Thermo-electrochemical study on the heat effects of $LiFePO_4$ lithium-ion battery during charge-discharge process. Int. J. Electrochem. Sci. *7*, 6571–6579.
18. Park, C.K., Park, S.B., Oh, S.H., Jang, H., and Cho, W.I. (2011). Li ion diffusivity and improved electrochemical performances of the carbon coated $LiFePO_4$. Bull. Korean Chem. Soc. *32*, 836–840.
19. Hong, L., Li, L., Chen-Wiegart, Y.-K., Wang, J., Xiang, K., Gan, L., Li, W., Meng, F., Wang, F., Wang, J., et al. (2017). Two-dimensional lithium diffusion behavior and probable hybrid phase transformation kinetics in olivine lithium iron phosphate. Nat. Commun. *8*, 1194.
20. Alibaba.com Price for acetonedicarboxylic acid. www.Alibaba.Com/showroom/1-3-acetonedicarboxylic-acid.Html.
21. Alibaba.com Price for citric acid. https://www.alibaba.com/showroom/citric-acid.html.
22. Adams, R., Chiles, H.M., and Rassweiler, C.F. (1925). Acetonedicarboxylic Acid. In Organic Syntheses (Wiley). https://doi.org/10.1002/0471264180.os005.03.
23. Borsook, H., and Keighley, G. (1933). Oxidation-reduction potential of ascorbic acid (vitamin C). Proc. Natl. Acad. Sci. USA. *19*, 875–878.
24. Kinyanjui, M.K., Axmann, P., Wohlfahrt-Mehrens, M., Moreau, P., Boucher, F., and Kaiser, U. (2010). Origin of valence and core excitations in $LiFePO_4$ and $FePO_4$. J. Phys. Condens. Matter *22*, 275501.
25. Laffont, L., Delacourt, C., Gibot, P., Wu, M.Y., Kooyman, P., Masquelier, C., and Tarascon, J.M. (2006). Study of the $LiFePO_4/FePO_4$ two-phase system by high-resolution electron energy loss spectroscopy. Chem. Mater. *18*, 5520–5529.
26. Andersson, A.S., and Thomas, J.O. (2001). The source of first-cycle capacity loss in $LiFePO_4$. J. Power Sources *97–98*, 498–502.
27. Delmas, C., Maccario, M., Croguennec, L., Le Cras, F.L., and Weill, F. (2008). Lithium deintercalation in $LiFePO_4$ nanoparticles via a domino-cascade model. Nat. Mater. *7*, 665–671.
28. Malik, R., Burch, D., Bazant, M., and Ceder, G. (2010). Particle size dependence of the ionic diffusivity. Nano Lett. *10*, 4123–4127.
29. Wang, T., Yu, X., Fan, M., Meng, Q., Xiao, Y., Yin, Y.-X., Li, H., and Guo, Y.-G. (2020). Direct regeneration of spent $LiFePO_4$ via a graphite prelithiation strategy. Chem. Commun. (Camb.) *56*, 245–248.
30. Paul, N., Wandt, J., Seidlmayer, S., Schebesta, S., Mühlbauer, M.J., Dolotko, O., Gasteiger, H.A., and Gilles, R. (2017). Aging behavior of lithium iron phosphate based 18650-type cells studied by in situ neutron diffraction. J. Power Sources *345*, 85–96.
31. Porcher, W., Moreau, P., Lestriez, B., Jouanneau, S., and Guyomard, D. (2008). Is $LiFePO_4$ stable in water? Electrochem. Solid State Lett. *11*, 4–8.
32. Chung, S.Y., Choi, S.Y., Yamamoto, T., and Ikuhara, Y. (2008). Atomic-scale visualization of antisite defects in $LiFePO_4$. Phys. Rev. Lett. *100*, 125502.
33. Lee, J., Zhou, W., Idrobo, J.C., Pennycook, S.J., and Pantelides, S.T. (2011). Vacancy-driven anisotropic defect distribution in the battery-cathode material $LiFePO_4$. Phys. Rev. Lett. *107*, 085507.

34. Han, X., Ouyang, M., Lu, L., and Li, J. (2014). A comparative study of commercial lithium ion battery cycle life in electric vehicle: capacity loss estimation. J. Power Sources *268*, 658–669.

35. DeRousseau, M., Gully, B., Taylor, C., Apelian, D., and Wang, Y. (2017). Repurposing used electric car batteries: a review of options. JOM *69*, 1575–1582.

36. Dai, Q., Gaines, L., Spangenberger, J., Kelly, J.C., Ahmed, S., and Wang, M. (2019). Everbatt: A closed-loop battery recycling cost and environmental impacts model. www.Anl.Gov/egs/everbatt.

37. Elwert, T., Hua, Q.S., and Schneider, K. (2019). Recycling of lithium iron phosphate batteries: future prospects and research needs. Mater. Sci. Forum *959*, 49–68.

38. Yu, J.Z., Wang, X., Zhou, M.Y., and Wang, Q. (2019). A redox targeting-based material recycling strategy for spent lithium ion batteries. Energy Environ. Sci. *12*, 2672–2677.

39. Wang, W., and Wu, Y. (2017). An overview of recycling and treatment of spent $LiFePO_4$ batteries in china. Resour. Conserv. Recycl. *127*, 233–243.

40. Cai, G., Fung, K.Y., Ng, K.M., and Wibowo, C. (2014). Process development for the recycle of spent lithium ion batteries by chemical precipitation. Ind. Eng. Chem. Res. *53*, 18245–18259.

41. Shin, E.J., Kim, S., Noh, J.-K., Byun, D., Chung, K.Y., Kim, H.-S., and Cho, B.-W. (2015). A green recycling process designed for $LiFePO_4$ cathode materials for Li-ion batteries. J. Mater. Chem. A *3*, 11493–11502.

42. Li, L., Bian, Y., Zhang, X., Yao, Y., Xue, Q., Fan, E., Wu, F., and Chen, R. (2019). A green and effective room-temperature recycling process of $LiFePO_4$ cathode materials for lithium-ion batteries. Waste Manag. *85*, 437–444.

43. Li, L., Lu, J., Zhai, L., Zhang, X., Curtiss, L., Jin, Y., Wu, F., Chen, R., and Amine, K. (2018). A facile recovery process for cathodes from spent lithium iron phosphate batteries by using oxalic acid. CSEE J. Power Energy Syst. *4*, 219–225.

44. Yang, Y., Meng, X., Cao, H., Lin, X., Liu, C., Sun, Y., Zhang, Y., and Sun, Z. (2018). Selective recovery of lithium from spent lithium iron phosphate batteries: a sustainable process. Green Chem. *20*, 3121–3133.

45. Li, X., Zhang, J., Song, D., Song, J., and Zhang, L. (2017). Direct regeneration of recycled cathode material mixture from scrapped $LiFePO_4$ batteries. J. Power Sources *345*, 78–84.

46. Song, X., Hu, T., Liang, C., Long, H.L., Zhou, L., Song, W., You, L., Wu, Z.S., and Liu, J.W. (2017). Direct regeneration of cathode materials from spent lithium iron phosphate batteries using a solid phase sintering method. RSC Adv. *7*, 4783–4790.

47. Li, J., Wang, Y., Wang, L., Liu, B., and Zhou, H. (2019). A facile recycling and regeneration process for spent $LiFePO_4$ batteries. J. Mater. Sci. Mater. Electron. *30*, 14580–14588.

48. Ganter, M.J., Landi, B.J., Babbitt, C.W., Anctil, A., and Gaustad, G. (2014). Cathode refunctionalization as a lithium ion battery recycling alternative. J. Power Sources *256*, 274–280.

49. An, K., Wang, X.L., and Stoica, A.D. (2012). Vdrive- Data Reduction and Interactive Visualization Software for Event Mode Neutron Diffraction, 1521–3773, p. 621.

50. Toby, B.H. (2001). Expgui, a graphical user interface for GSAS. J. Appl. Crystallogr. *34*, 210–213.

51. Pacioni, N.L., Borsarelli, C.D., Rey, V., and Veglia, A.V. (2015). In Silver Nanoparticle Applications: in the Fabrication and Design of Medical and Biosensing Devices, Springer International Publishing, Silver Nanoparticle Applications, E. Alarcon, M. Griffith, and K.I. Udekwu, eds. (Springer International Publishing).

52. Hu, B., and Tao, G. (2015). Molecular dynamics simulations on lithium diffusion in $LiFePO_4$: the effect of anti-site defects. J. Mater. Chem. A *3*, 20399–20407.

53. Pachauri, R.K., and Meyer, L. (2014). Climate Change 2014: Synthesis Report (Intergovernmental Panel on Climate Change).